

**Charged pion production in 2A to 8A GeV central Au+Au Collisions**

J. L. Klay,<sup>1</sup> N. N. Ajitanand,<sup>2</sup> J. M. Alexander,<sup>2</sup> M. G. Anderson,<sup>1</sup> D. Best,<sup>3</sup> F. P. Brady,<sup>1</sup> T. Case,<sup>3</sup> W. Caskey,<sup>1</sup> D. Cebra,<sup>1</sup> J. L. Chance,<sup>1</sup> P. Chung,<sup>2</sup> B. Cole,<sup>4</sup> K. Crowe,<sup>3</sup> A. C. Das,<sup>5</sup> J. E. Draper,<sup>1</sup> M. L. Gilkes,<sup>6</sup> S. Gushue,<sup>7</sup> M. Heffner,<sup>1</sup> A. S. Hirsch,<sup>6</sup> E. L. Hjort,<sup>6</sup> L. Huo,<sup>8</sup> M. Justice,<sup>9</sup> M. Kaplan,<sup>10</sup> D. Keane,<sup>9</sup> J. C. Kintner,<sup>11</sup> D. Krofcheck,<sup>12</sup> R. A. Lacey,<sup>2</sup> J. Lauret,<sup>2</sup> C. Law,<sup>2</sup> M. A. Lisa,<sup>5</sup> H. Liu,<sup>9</sup> Y. M. Liu,<sup>8</sup> R. McGrath,<sup>2</sup> Z. Milosevich,<sup>10</sup> G. Odyniec,<sup>3</sup> D. L. Olson,<sup>3</sup> S. Y. Panitkin,<sup>9</sup> C. Pinkenburg,<sup>2</sup> N. T. Porile,<sup>6</sup> G. Rai,<sup>3</sup> H. G. Ritter,<sup>3</sup> J. L. Romero,<sup>1</sup> R. Scharenberg,<sup>6</sup> B. Srivastava,<sup>6</sup> N. T. B. Stone,<sup>3</sup> T. J. M. Symons,<sup>3</sup> S. Wang,<sup>9</sup> R. Wells,<sup>5</sup> J. Whitfield,<sup>10</sup> T. Wienold,<sup>3</sup> R. Witt,<sup>9</sup> L. Wood,<sup>1</sup> and W. N. Zhang<sup>8</sup>  
(E895 Collaboration)

<sup>1</sup>University of California, Davis, California 95616, USA

<sup>2</sup>Department of Chemistry and Physics, SUNY, Stony Brook, New York 11794-3400, USA

<sup>3</sup>Lawrence Berkeley National Laboratory, Berkeley, California 94720, USA

<sup>4</sup>Columbia University, New York, New York 10027, USA

<sup>5</sup>The Ohio State University, Columbus, Ohio 43210, USA

<sup>6</sup>Purdue University, West Lafayette, Indiana 47907-1396, USA

<sup>7</sup>Brookhaven National Laboratory, Upton, New York 11973, USA

<sup>8</sup>Harbin Institute of Technology, Harbin, 150001 People's Republic of China

<sup>9</sup>Kent State University, Kent, Ohio 44242, USA

<sup>10</sup>Carnegie Mellon University, Pittsburgh, Pennsylvania 15213, USA

<sup>11</sup>St. Mary's College of California, Moraga, California 94575, USA

<sup>12</sup>University of Auckland, Auckland, New Zealand

(Received 1 July 2003; published 26 November 2003)

Momentum spectra of charged pions over nearly full rapidity coverage from target to beam rapidity have been extracted from 0–5% most central Au+Au collisions in the beam energy range from 2A to 8A GeV by the E895 experiment. Using a thermal parametrization to fit the transverse mass spectra, rapidity density distributions are extracted. The observed spectra are compared with predictions from the RQMD version 2.3 cascade model and also to a thermal model including longitudinal flow. The total  $4\pi$  yields of the charged pions are used to infer an initial-state entropy produced in the collisions.

DOI: 10.1103/PhysRevC.68.054905

PACS number(s): 25.75.-q, 25.60.Gc

**I. INTRODUCTION**

One of the primary goals of the study of heavy ion collisions at relativistic energies is the improvement of our understanding of the bulk properties of nuclear/hadronic matter at high temperatures and densities. As a first step in understanding these properties, one should carefully characterize the particle species that make up the bulk of the matter. For the energy regime of the Bevalac/SIS (0.2A to 1.2A GeV), collisions between heavy nuclei cause a compression of the nuclear matter, resulting in a disassembly into the constituent neutrons and protons, which are emitted either individually or bound within various light composite fragments ( $d$ ,  $t$ ,  $^3\text{He}$ ,  $^4\text{He}$ ) [1,2].

At the top energy for Alternating Gradient Synchrotron (AGS) Au+Au collisions of 10.8A GeV, the most copiously produced charged particles are the lightest of the mesons, the pions [3,4]. The matter has evolved from a heated and compressed gas of nucleons into a hot dense gas of hadrons, predominantly  $\pi$ -mesons. Thus the energy region from 2A to 8A GeV represents a transition regime. Studies of nuclear stopping suggest the maximum density achieved increases from three times normal nuclear density at 1A GeV [5–7] to eight times normal nuclear density at 10A GeV [8]. Measurements of the proton directed and elliptic flow indicate that hydrodynamic flow has saturated across this energy range

and cannot account for the increased energy available [9,10]. This additional available energy goes primarily into pion production. By studying the pion production across this regime we are able to observe nuclear matter in transition.

Early on, in the study of heavy ion collisions, an enhanced yield of pions was seen as a possible signature of a transition to a deconfined state of matter. However, in the early studies of pion yields in the 1A GeV energy range at the Bevalac [11–13], it was observed that the measured pion production cross sections were smaller than predicted at the time. This observation led to the conjecture, which was later experimentally demonstrated, that the excess kinetic energy was converted into hydrodynamical flow effects. The strong radial flow observed at this energy implies a significant expansion and cooling, which limits the freeze-out pion multiplicities [14,15]. More recently, more detailed measurements of the pion yields from 1A GeV Au+Au collisions have become available from the SIS experiments [16–19]. These results demonstrate a roughly two to one ratio of  $\pi^-$  over  $\pi^+$  and a strong nonthermal low- $p_t$  enhancement. Both features are strong indicators that pions at this energy are produced almost exclusively through the  $\Delta$  resonance [20]. In full energy AGS collisions (Au+Au at 10.8A GeV), pion production has been studied at midrapidity [3] and at target rapidity [21]. Although there is still an asymmetry between  $\pi^-$  and  $\pi^+$  production and there is also still evidence of a low- $p_t$  en-

hancement in the momentum spectra, these effects are much less significant than at SIS. The broad rapidity coverage for both pions and protons at these energies has also been used to study the development of longitudinal flow [22].

This paper will detail the development of pion production across the beam energy range from 2A to 8A GeV. The role of the  $\Delta$  resonance production mechanism will be explored through observations of the overall pion ratios and through Relativist Quantum Molecular Dynamics (RQMD) simulations [41]. The rapidity density distributions will be used with previously published proton rapidity distributions [23] to explore the effects of collective longitudinal flow. The overall pion multiplicities will be used to establish a low energy base line for a recent pion multiplicity based quark gluon plasma (QGP) search at the CERN SPS [24].

## II. DATA COLLECTION AND ANALYSIS

The data were taken at the Brookhaven National Laboratory AGS by the E895 experiment using the EOS time projection chamber (TPC) [25] during a series of runs in 1996. This paper presents charged pion transverse mass and rapidity density spectra from Au+Au collisions at nominal beam energies of 2, 4, 6, and 8 GeV/nucleon(A GeV). (After correcting for energy loss before the target, the actual beam energies of collisions at 2A and 4A GeV were found to be 1.85A and 3.91A GeV, respectively. No corrections were necessary for 6A and 8A GeV). The EOS TPC provides nearly  $4\pi$  solid angle coverage, which makes global characterization of the collision events possible. Charged particle momenta are reconstructed from the helical trajectories of tracks reconstructed from the ionization trails left by particles passing through the TPC, which was situated inside the Multi-Particle Spectrometer (MPS) magnet. Data presented for 2A GeV collisions were taken in a 0.75 T field, while 4A, 6A, and 8A GeV collisions were taken in a 1 T field.

A primary track multiplicity for each event is obtained by rejecting those tracks which do not pass within 2.5 cm of the reconstructed event vertex in the target. The multiplicity distribution from a minimum trigger-biased sample of events is used to discriminate event centrality classes by assuming a monotonic relationship between the impact parameter and multiplicity [26]. The data presented in this paper are selected on the top 5% most central events; an ensemble of  $\approx 20000$  events at each energy for this centrality selection were analyzed to obtain the spectra.

Identification of particle species is determined via multiple sampling (up to 128 samples) of the ionization in P10 (10% methane, 90% argon) drift gas. The average ionization energy loss  $\langle dE/dx \rangle$  is computed for each track from the available samples via a truncated mean to reduce the influence of the large energy tail of the distribution. The 20% highest  $dE/dx$  samples are discarded from the calculation of the average.

Figure 1 shows a typical particle identification map with  $\langle dE/dx \rangle$  plotted versus reconstructed track rigidity ( $=p/Z$ ) at 6A GeV. The various particle species are identified by their separation into bands. The pion spectra were obtained by fitting projections of the  $\langle dE/dx \rangle$  in narrow bins of  $m_t - m_0$

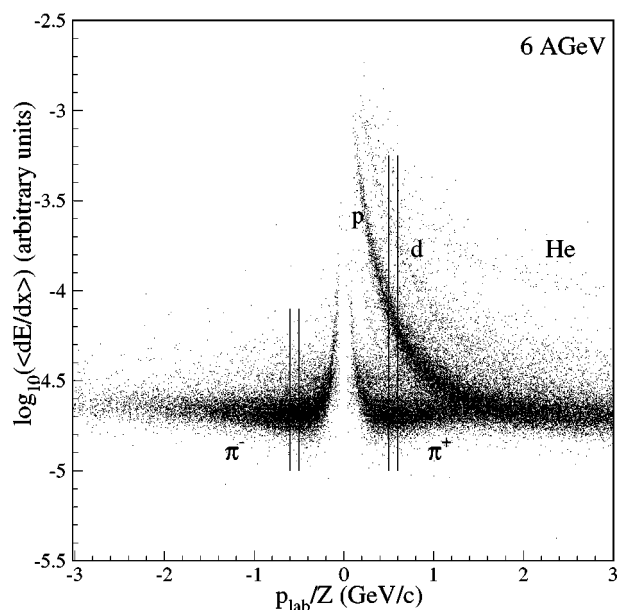


FIG. 1.  $\langle dE/dx \rangle$  as a function of rigidity at 6A GeV. A parametrized Bethe-Bloch prediction is used to fix the mean energy loss for each particle species as a function of rigidity. The narrow slices illustrate the location of the  $\langle dE/dx \rangle$  projections shown in Fig. 2.

and rapidity, using an assumption of the pion mass and charge to calculate the  $(m_t - m_0, y)$  coordinates for a given measured particle  $(p_x, p_y, p_z)$ .

The single-particle  $\langle dE/dx \rangle$  projections are often described by a Gaussian distribution centered on the mean value predicted by a Bethe-Bloch formulation. However, this assumes that the calculation of  $\langle dE/dx \rangle$  for each track was obtained in an identical fashion for all tracks in the distribution. In fact, the truncated mean method used in this analysis introduces a skewing toward larger  $\langle dE/dx \rangle$  which comes from combining tracks of different number of samples,  $N_{hits}$ . One way to avoid this skewing is to divide the data into bins of  $N_{hits}$ , which reduces the effect. However the reduction in statistics for each bin leads to increased uncertainty in the determined yields. Therefore, for this analysis, a model of the  $N_{hits}$ -integrated single-particle  $\langle dE/dx \rangle$  distribution shapes was used with the predicted mean values from a Bethe-Bloch parametrization of the  $\langle dE/dx \rangle$  as a function of  $\beta\gamma$  to extract the total yields of pions from each projection. The model is represented by a correlated sum of Gaussian distributions: a main Gaussian for the bulk of the distribution plus a smaller, offset “shoulder” Gaussian for the high- $\langle dE/dx \rangle$  tail. The parameters of the model were studied as a function of beam energy, particle type, and  $(m_t - m_0, y)$  bin in regions where the single-particle distributions can be separately characterized. Tight constraints on the model parameters were applied in order to extrapolate the model into regions where multiple-particle distributions partially overlap. Thus the relative yields of different particles were deconvoluted in each  $(m_t - m_0, y)$  bin: 0.1 unit rapidity slices over the full rapidity range from target to beam rapidity, with the midrapidity bin covering the range  $-0.05 < y_{c.m.} < 0.05$ , and in 25 MeV/c<sup>2</sup> bins in  $m_t - m_0$  in the range  $0 < m_t - m_0 < 1.0$  GeV/c<sup>2</sup>. Particles

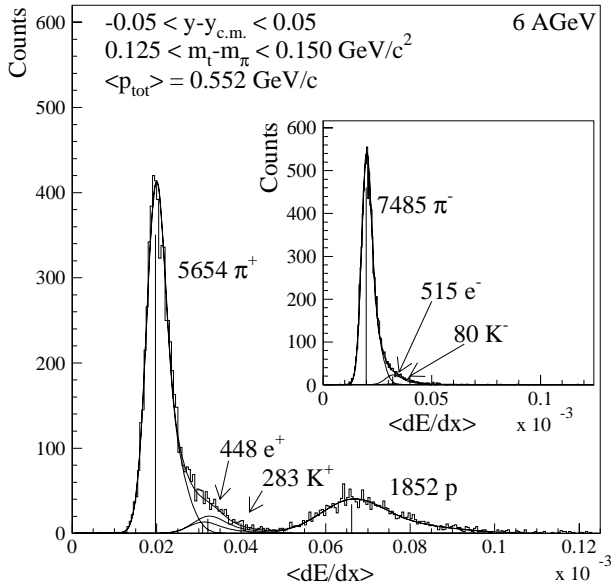


FIG. 2. Projections of the positive and negative (inset) particles  $\langle dE/dx \rangle$  at midrapidity and  $0.125 < m_t - m_0 < 0.150 \text{ GeV}/c^2$ , in the rigidity ranges indicated on Fig. 1. The  $(m_t - m_0, y)$  ranges were calculated assuming the pion mass. The function used to fit the data is the two-Gaussian model (described in the text) of the single-particle  $\langle dE/dx \rangle$  distributions, one for each particle type. The integrals under the pion peaks are the total yield for the fitted  $(m_t - m_0, y)$  bin and the contributions from all other particles are discarded.

of the wrong mass and/or charge contaminating the pion sample in a given  $(m_t - m_0, y)$  bin were discarded.

Figure 2 shows an example of a single  $(m_t - m_0, y)$  slice at midrapidity for 6A GeV and  $0.125 < m_t - m_0 < 0.150 \text{ GeV}/c^2$ . The total yields are obtained by integrating the area under the fitted distributions for each particle. Oppositely charged particles are projected separately. The inset shows the projection of negatively charged particles, which are well characterized by this method of particle identification over the entire range of transverse mass and rapidity. However, as the rapidity and transverse mass increase, the positively charged pions suffer increasing contamination due to the overlap with the positive kaons and protons. The range of  $m_t - m_0$  and rapidity over which the  $\pi^+$  yields are extracted is therefore more limited.

Electron contamination was estimated by studying their yields in the regions of phase space where they are relatively cleanly identified (for  $p_{lab} < 150 \text{ MeV}/c$  and  $300 < p_{lab} < 500 \text{ MeV}/c$ ) and interpolating between these limits. It was found that electrons contribute  $\approx 10\%$  to the observed yield of pions for lab momenta  $150 < p_{lab} < 250 \text{ MeV}/c$ . Since the electron yields fall significantly as a function of their own transverse momentum, the contamination predominantly affects the lowest pion  $m_t - m_0$  bins. The errors on the quoted pion yields account for possible systematic uncertainties in the determination of the electron contamination.

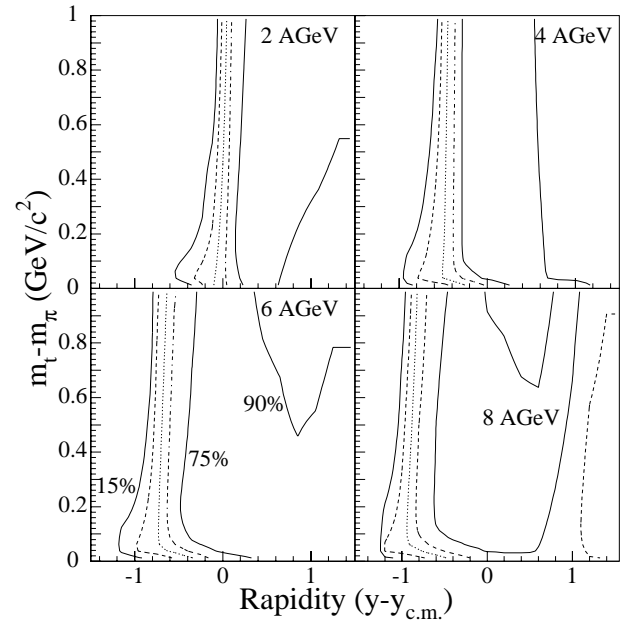


FIG. 3. EOS TPC total “efficiency” ( $\equiv 1/\text{correction}$ , including effects of acceptance, tracking efficiency, and momentum resolution) for pions produced in 2A, 4A, 6A, and 8A GeV 0–5% central Au+Au collisions. The efficiencies are obtained from GEANT simulations of the detector response to Monte Carlo tracks embedded into real data events and propagated through the reconstruction chain. The contours, shown in steps of  $\sim 15\%$ , include the effects of geometric acceptance, tracking efficiency, and momentum resolution.

Observed kaon yields from the same beam energy range, measured by E866/E917 [27,28], folded with the EOS TPC detector response allow us to extend the reach of the  $\pi^+$  fitting out to  $p_{lab} \sim 1.2 \text{ GeV}/c$ . For lab momenta above  $1.2 \text{ GeV}/c$ , however, the  $\pi^+$  become hopelessly entangled with the protons, which are approaching minimum ionizing  $\langle dE/dx \rangle$ . This cutoff manifests at different  $m_t - m_0$ , depending on the rapidity and bombarding energy.

Detector response to the final-state collision products has been extensively studied using the GEANT 3.21 simulation package. Small (maximum of four per event) samples of pions with momentum distributions approximating the real data are embedded into full data events. These particles are tagged and propagated through the data reconstruction chain to determine the effects of detector acceptance, tracking efficiency, and momentum resolution.

Since the beam actually passes through the sensitive volume of the detector, there is no explicit low- $p_t$  measurement cutoff. However, forward-focusing causes increased tracking losses at low  $p_t$  and forward rapidities due to higher track densities and track merging. Losses at backward rapidities and high  $m_t - m_0$  are dominated by the geometric acceptance of the detector, while at more forward rapidities, the high  $m_t - m_0$  tracks are stiffer and therefore suffer from worsening momentum resolution. Figure 3 shows the overall detection efficiency obtained from simulations as a function of  $m_t$

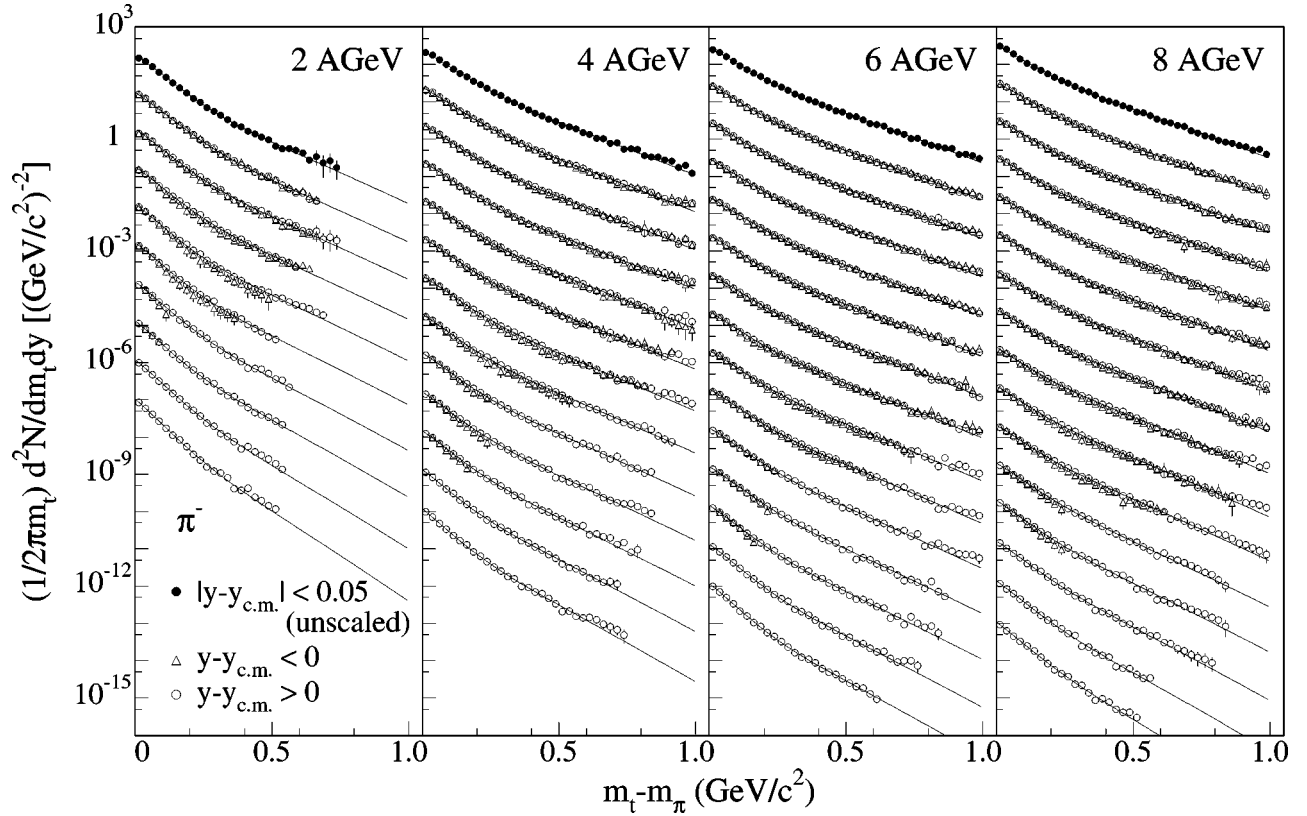


FIG. 4. Invariant yield per event as a function of  $m_t - m_0$  for  $\pi^-$  at 2A, 4A, 6A, and 8A GeV. Midrapidity is shown unscaled, while the 0.1 unit forward/backward rapidity slices are scaled down by successive factors of 10. The functions plotted with the data are two-slope Boltzmann parametrizations described in the text.

$-m_0$  and rapidity for pions at each beam energy. The contours indicate steps of  $\sim 15\%$ . The raw data are corrected for these effects to extract the total yields of positive and negative pions as a function of  $m_t - m_0$  and rapidity at each beam energy.

Due to the large acceptance of our device, we can test the systematic uncertainties on the yields by comparing forward and backward rapidity corrected spectra. Overlapping acceptances at 2, 4, 6 and 8 GeV allow us to conclude that rapidity bins corresponding to  $y_{lab} < 0.5$  are most affected by the systematic uncertainties in our corrections. The underestimated corrections in this region of phase space are not surprising given that neither detector performance nor detector simulations were optimized for target rapidity in the lab frame. Here tracks cross the fewest pad rows and have the smallest radii of curvature. Midrapidity yields at all four beam energies were checked against published results from E866/E917 [29,30]. The average level of agreement between our spectra and E866/E917 over all  $m_t - m_0$  and beam energies is observed to be  $\approx 7\%$ . The minimum systematic uncertainties at all rapidities for the E895 data presented here are estimated to be 5%, while for the most backward rapidity bins, the uncertainties at high  $m_t - m_0$  can become as large as 50%. These errors are included on the spectra reported in this paper.

### III. RESULTS

Figures 4 and 5 show the fully corrected, invariant yields of charged pions per event from 0–5% central Au+Au collisions at 2A, 4A, 6A, and 8A GeV. Midrapidity is shown unscaled as black circles, while each bin forward/backward of midrapidity is scaled down by a successive factor of 10. Forward rapidities are indicated as open circles and backward rapidities as open triangles. The reported error bars include both statistical and systematic uncertainties.

The approximately exponential decay of the particle yields as a function of transverse mass has been observed in high energy particle and heavy ion experiments over a wide range of conditions. In order to extract the full  $4\pi$  yields of pions (including those from resonance feed-down) produced in the beam energy range studied here, a simple parametrization of the pion  $m_t - m_0$  spectra which reproduces the observed shapes of the spectra over the full range of  $m_t - m_0$ , from 0 to 1  $\text{GeV}/c^2$  is used. This parametrization is the sum of two independent Maxwell-Boltzmann thermal functions, each term of which can be expressed in terms of the measured coordinates  $(m_t - m_0, y)$ , integrated over azimuth as

$$\frac{1}{2\pi m_t} \frac{d^2 N}{dm_t dy} = A(y) m_t e^{-(m_t - m_0)/T_{eff}(y)}, \quad (1)$$

where the amplitude  $A$  and inverse slope parameter  $T_{eff}$  are parameters that can be extracted from fits to the data at

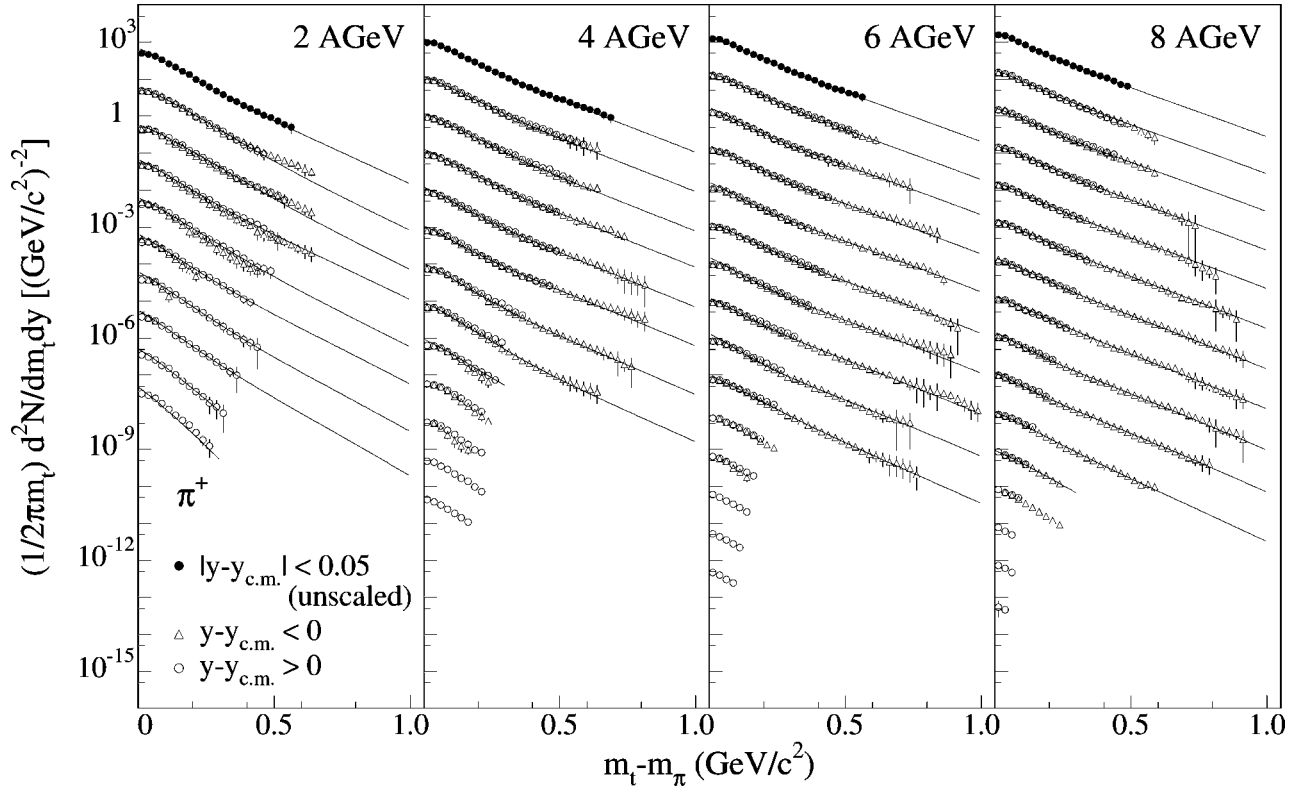


FIG. 5. Invariant yield per event as a function of  $m_t - m_0$  for  $\pi^+$  at 2A, 4A, 6A, and 8A GeV. Midrapidity is shown unscaled, while the 0.1 unit forward/backward rapidity slices are scaled down by successive factors of 10. The functions plotted with the data are two-slope Boltzmann parametrizations described in the text.

each rapidity slice. Integration of either of these two distributions over  $m_t$  produces its contribution to the total number of particles per unit of rapidity in the given rapidity slice [31],

$$\frac{dN}{dy}(y) = 2\pi A(y)[m_0^2 T_{eff}(y) + 2m_0 T_{eff}^2(y) + 2T_{eff}^3(y)]. \quad (2)$$

Note that  $A(y)$  in Eq. (1) can be rewritten in terms of  $dN/dy(y)$ , using Eq. (2).

The low- $p_t$  enhancement observed in the pion yields has been attributed to feed-down from late-stage resonance decays [32–34], which tend to populate lower pion  $p_t$  in the frame of the collision due to the nature of the decay kinematics. In particular, at the beam energies presented here, the  $\Delta$  resonances [such as the  $\Delta(1232)$ ] are the predominant mechanism for pion production, due to the very large cross section for pion-nucleon interactions. The observed asymmetry in the spectral shapes of positive and negative pions at low  $m_t - m_0$  has been described elsewhere by a final-state Coulomb interaction of the pions with the nuclear fireball [35–37].

The two-slope model that has been applied to the pion spectra was chosen to provide the simplest phenomenological description of the data. Since this parametrization does reasonably well at describing the observed shapes of the spectra over all  $m_t - m_0$ , it is used to extract the  $4\pi$  yields of pions in these collisions with minimal extrapolation,

$$\frac{1}{2\pi m_t} \frac{d^2N}{dm_t dy} = \frac{dN/dy_1 m_t e^{-(m_t - m_0)/T_1}}{2\pi T_1 (m_0^2 + 2m_0 T_1 + 2T_1^2)} + \frac{dN/dy_2 m_t e^{-(m_t - m_0)/T_2}}{2\pi T_2 (m_0^2 + 2m_0 T_2 + 2T_2^2)}. \quad (3)$$

The four parameter fit includes two independently fit inverse slope parameters [ $T_1(y)$ ,  $T_2(y)$ ], and two independently fit yield parameters [ $dN/dy_1(y)$ ,  $dN/dy_2(y)$ ], which reasonably describe the low- $(m_t - m_0)$  and high- $(m_t - m_0)$  portions of the spectrum at each rapidity. These fits are shown as solid lines in Figs. 4 and 5. The data at more forward rapidities, where in particular the  $\pi^+$  spectra are limited to the range  $m_t - m_0 < 200$  MeV/c, are not fit with the two-slope parametrization.

More detailed examples of these two-slope fits at midrapidity are shown in Fig. 6. Figures 7–10 show the four fit parameters as a function of rapidity from the  $\pi^-$  spectra and the resulting total  $dN/dy$ . The parameters plotted in the top row are from fits in which all four parameters are allowed to be free. All of them show an approximately Gaussian dependence on rapidity, which is demonstrated by the solid line in each panel. The bottom row of each figure demonstrates the result of a second fit of the spectra in which the high- $(m_t - m_0)$  inverse slope parameter is constrained to the Gaussian (solid line) value. This procedure smooths out the covariance between the individual yield parameters but has a negligible effect on total  $dN/dy$  (the rightmost panel).

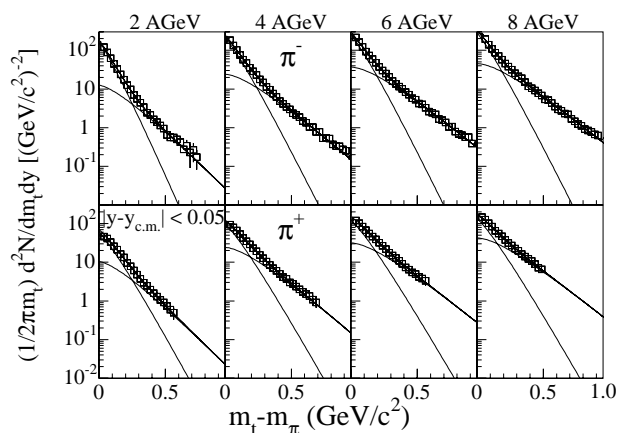


FIG. 6. Pion transverse mass spectra at midrapidity for 2A, 4A, 6A, and 8A GeV (uppermost curves on Figs. 4 and 5). Two-slope thermal fits are shown superposed on the data along with the contributions to the total from the two separate inverse slope terms in Eq. (3).

If the source of pions were a static thermal source of temperature  $T_0$  and zero chemical potential, the expected shape of  $T_{eff}$  in Figs. 7–11 would be  $T_0/\cosh(y)$ . [There would then be needed only a single term in Eq. (3).] We have shown in Ref. [23] that there is significant longitudinal flow, i.e., the source is not static. As the main purpose of the fits in Figs. 4 and 5 is for integration of the  $(m_t - m_0, y)$  spectra to obtain  $4\pi$  yields, a Gaussian fit of the inverse slope parameters in Figs. 7–11, rather than  $1/\cosh(y)$ , was used.

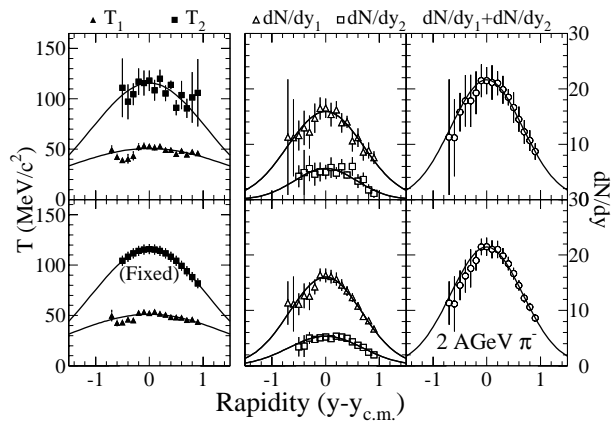


FIG. 7. Rapidity dependence of the fit parameters from 2A GeV  $\pi^- m_t - m_0$  spectra fits with a two-slope model. The left-most panels show the inverse slope parameters.  $T_1$  (indicated by closed triangles) dominates the low- $(m_t - m_0)$  range of the spectra, whereas  $T_2$  (indicated by closed squares) dominates the high- $(m_t - m_0)$  end of the spectra. The middle panels show the two  $dN/dy$  fit parameters ( $dN/dy_1$  in open triangles and  $dN/dy_2$  in open squares) and the rightmost panels show the total  $dN/dy$ , which is the sum of  $dN/dy_1$  and  $dN/dy_2$ . The top row reports the fit results when all four parameters are allowed to be independent in the fit. The bottom row shows the results for the remaining three parameters when the high- $(m_t - m_0)$  inverse slope is fixed to the Gaussian estimation. Note that the total  $dN/dy$  is fairly insensitive to the interplay among the parameters.

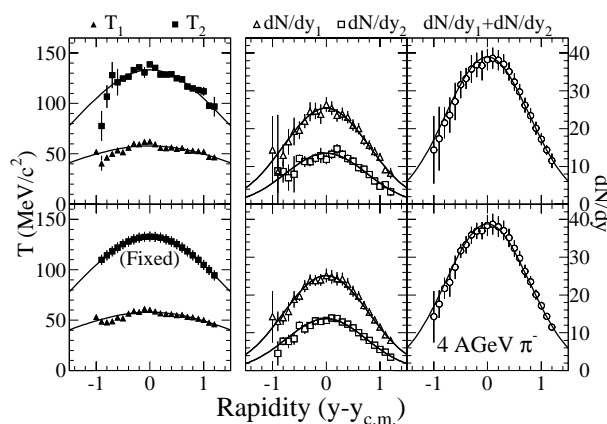


FIG. 8. Rapidity dependence of the fit parameters from 4A GeV  $\pi^- m_t - m_0$  spectra fits with a two-slope model. See caption of Fig. 7 for details.

Figure 11 shows the  $\pi^+$  fit parameters at each beam energy. The limited range in  $m_t - m_0$  of the  $\pi^+$  spectra is caused by the  $\langle dE/dx \rangle$  overlap with the protons, which makes it impossible to get good spectral data in all rapidity slices. In order to make reasonable estimates of the  $4\pi$  positive pion yields, the high- $(m_t - m_0)$  positive pion inverse slope parameters were assumed to be the same as those of the negative pions [16]. In the estimation of the  $\pi^+ dN/dy$ , the high- $(m_t - m_0)$  inverse slopes were therefore fixed to the negative pion values. Experimentally, the  $m_t - m_0$  negative pion inverse slope parameters do reasonably reproduce the observed high- $(m_t - m_0)$  positive pion inverse slopes in the rapidity regions where they can be measured. Where the  $m_t - m_0$  spectra are severely truncated, the positive pion yields were obtained from single-slope fits. The reported systematic uncertainties in these rapidity slices are correspondingly larger to account for this missed yield.

Figure 12 shows the beam energy dependence of the rapidity distributions of the negative and positive pions extracted from the fits. These distributions are well described by Gaussians, which are used to obtain the total  $4\pi$  yields by integrating the fitted distributions over all rapidity.

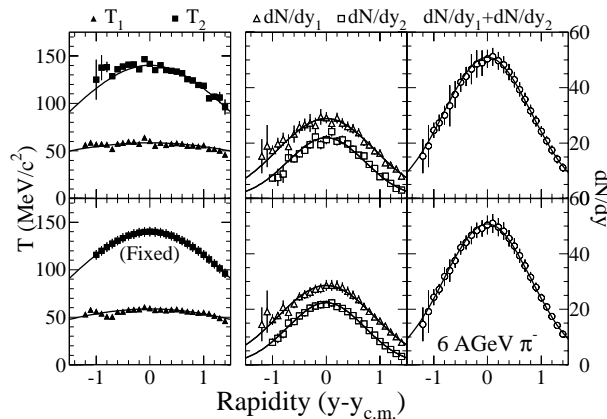


FIG. 9. Rapidity dependence of the fit parameters from 6A GeV  $\pi^- m_t - m_0$  spectra fits with a two-slope model. See caption of Fig. 7 for details.

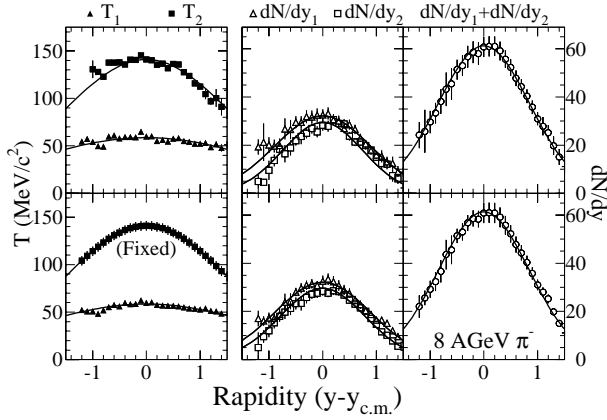


FIG. 10. Rapidity dependence of the fit parameters from 8A GeV  $\pi^-$   $m_t$ - $m_0$  spectra fits with a two-slope model. See caption of Fig. 7 for details.

$$\langle \pi \rangle = \int_{-\infty}^{+\infty} \frac{dN}{dy} dy = \sqrt{2\pi} w Q, \quad (4)$$

where  $Q$  is the value of  $dN/dy$  at  $y-y_{c.m.}=0$  and  $w$  is the width. The fit parameters and their uncertainties are listed in Tables I and II. Both the widths and the overall yields of pions increase as a function of beam energy. However, there is a more significant increase in the observed pion yields between 2A and 4A GeV than between 4A and 6A GeV or 6A and 8A GeV.

#### IV. DISCUSSION

In this section, some of the characteristics of the observed pion spectra obtained from E895 are discussed. The pion

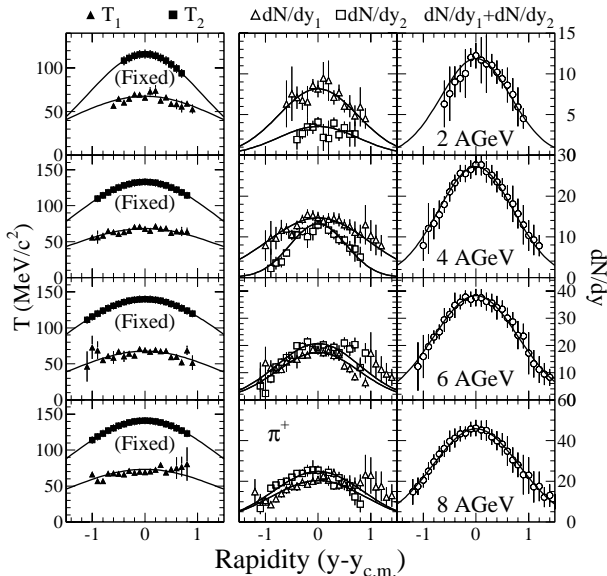


FIG. 11. Rapidity dependence of the fit parameters for each beam energy from the  $\pi^+$   $m_t$ - $m_0$  spectra fits with a two-slope model. (See caption of Fig. 7 for more details.) The high- $(m_t-m_0)$  inverse slope parameters have been fixed to the  $\pi^-$  parametrized values.

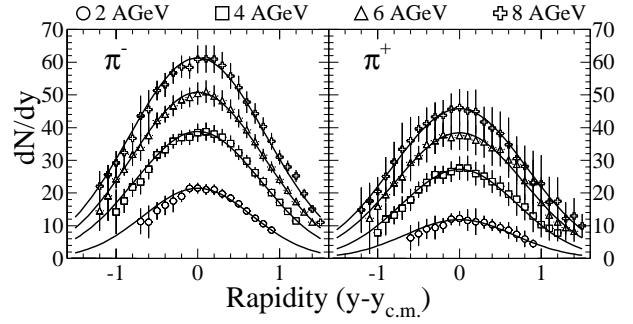


FIG. 12. Yield per event of  $\pi^-$  (left-hand panel) and  $\pi^+$  (right-hand panel) in 0–5% central Au+Au collisions at 2A, 4A, 6A, and 8A GeV integrated over  $m_t-m_0$  as a function of rapidity. A Gaussian parametrization is applied to extract the  $4\pi$  yields. Reported uncertainties are statistical plus systematic.

spectral shapes are compared to the predictions of a microscopic transport model, the  $dN/dy$  distributions are evaluated in the context of collective dynamics, and the overall yields are used to infer the initial-state entropy density obtained in these collisions.

It is interesting to note the asymmetry between the positive and negative pion yields at each beam energy. Although the ratio of negative to positive pions decreases over the studied beam energy range, from 1.88 at 2A GeV to 1.36 at 8A GeV (see Tables I and II), it does not reach the asymptotic value of  $\sim 1.0$  observed at the top CERN SPS energy [38,24]. The neutron excess in Au+Au collisions (118+118 neutrons compared to 79+79 protons) combined with the pion branching ratios suggests that 1.95 negative pions for every positive pion will be produced [13]. If the isospin fractions are folded with the observed cross sections for  $NN \rightarrow NN \pi$  from experimental measurements [39], the expected ratio of  $\langle \pi^- \rangle : \langle \pi^+ \rangle$  at 1A GeV is  $\sim 1.91:1$ . The 2A GeV data, with  $\sqrt{s_{NN}}$  not far from the  $\Delta(1232)$  production threshold, are quite near, though a little lower than this predicted ratio. As the energy increases, the number of directly produced pion pairs ( $\pi^- \pi^+$ ) is expected to lower the ratio, asymptotically approaching 1.0, which is the trend we observe. At 8A GeV the negative pion excess is only  $\approx 36\%$ , compared to 88% at 2A GeV.

#### A. RQMD comparisons

RQMD version 2.3 [40] is a microscopic transport model which attempts to simulate heavy ion collisions by propagat-

TABLE I.  $dN/dy$  fit parameters for negative pions at each beam energy with statistical and systematic uncertainties reported separately.  $Q_{\pi^-}$  is the amplitude of the distribution at  $y-y_{c.m.}=0$ ,  $\langle \pi^- \rangle$  is the  $4\pi$  yield (total area), and  $w_{\pi^-}$  is the width.

| $E_{beam}$ | $Q_{\pi^-}$              | $\langle \pi^- \rangle$   | $w_{\pi^-}$                   |
|------------|--------------------------|---------------------------|-------------------------------|
| 2A GeV     | 21.3 $\pm$ 0.1 $\pm$ 1.3 | 36.1 $\pm$ 0.3 $\pm$ 2.0  | 0.675 $\pm$ 0.006 $\pm$ 0.005 |
| 4A GeV     | 39.0 $\pm$ 0.1 $\pm$ 2.1 | 76.0 $\pm$ 0.2 $\pm$ 4.2  | 0.780 $\pm$ 0.003 $\pm$ 0.002 |
| 6A GeV     | 50.8 $\pm$ 0.1 $\pm$ 2.7 | 104.0 $\pm$ 0.2 $\pm$ 5.4 | 0.817 $\pm$ 0.002 $\pm$ 0.001 |
| 8A GeV     | 61.1 $\pm$ 0.1 $\pm$ 3.3 | 130.7 $\pm$ 0.4 $\pm$ 7.9 | 0.854 $\pm$ 0.003 $\pm$ 0.008 |

TABLE II.  $dN/dy$  fit parameters for positive pions at each beam energy with statistical and systematic uncertainties reported separately.  $Q_{\pi^+}$  is the amplitude of the distribution at  $y-y_{c.m.}=0$ ,  $\langle\pi^+\rangle$  is the  $4\pi$  yield (total area), and  $w_{\pi^+}$  is the width.

| $E_{beam}$ | $Q_{\pi^+}$                  | $\langle\pi^+\rangle$        | $w_{\pi^+}$                 |
|------------|------------------------------|------------------------------|-----------------------------|
| 2A GeV     | $11.5 \pm 0.3 \pm 1.2$       | $19.2 \pm 1.3^{+2.0}_{-1.0}$ | $0.668 \pm 0.053 \pm 0.011$ |
| 4A GeV     | $27.7 \pm 0.3^{+1.2}_{-1.4}$ | $46.3 \pm 0.8^{+4.5}_{-3.3}$ | $0.667 \pm 0.015 \pm 0.025$ |
| 6A GeV     | $38.4 \pm 0.3^{+2.4}_{-1.8}$ | $75.7 \pm 1.1^{+3.4}_{-2.9}$ | $0.787 \pm 0.014 \pm 0.016$ |
| 8A GeV     | $46.2 \pm 0.4^{+2.7}_{-3.4}$ | $95.9 \pm 1.1^{+6.1}_{-5.9}$ | $0.828 \pm 0.013 \pm 0.005$ |

ing individually all particles through the six dimensions of phase space in the fireball. Interaction probabilities are approximated by using published interaction cross sections of free hadrons and the relative phase space proximity of pairs of particles at each time step of the reaction. Inelastic collisions may produce new particles, such as pions, which are also propagated through phase space along with the nucleons. The reaction ends when the phase space density reaches a low enough threshold such that the probability of further interactions is small—the freeze-out point. This model has been reasonably successful in describing many final-state observables experimentally measured in the beam energy range studied for this analysis [41].

In this and other cascade models, final-state particle distributions are frozen at the end of the reaction. Post-freeze-out effects, such as the Coulomb interaction of the pions with the nuclear fireball, are not included. However, RQMD combined with an afterburner to simulate final-state Coulomb interactions [42] and to permit the decay of residual resonances has been successful at describing asymmetries in observed pion yields at low  $p_t$ .

RQMD version 2.3, with the nucleon mean field setting turned on, was used to generate pion distributions from central ( $b \leq 3$  fm) Au+Au collisions for comparison with the data obtained by E895 for this paper. One of the output parameters from RQMD records the nature of the last collision, “lastcl,” of each particle before freeze-out. Particles whose lastcl was a thermal rescattering are labeled “thermal.” Particles whose lastcl was the decay of a resonance have the parent particle listed explicitly. However, high mass resonances which are not  $\Delta$ ’s or vector mesons are combined in a single category labeled “himass” in the user’s notes for the code. Particles whose lastcl was string or rope fragmentation are indicated separately. Figures 13 and 14 show the nature of the last collision for  $\pi^-$  and  $\pi^+$  for a centrality selection of  $b \leq 3$  fm at 2A GeV and 8A GeV, respectively. The distributions are normalized to the per event yield of pions. In each case, the  $\Delta$  resonances are the largest single contributor to the last pion interactions before freeze-out.

The dependence of the pion spectral shapes on feed-down from  $\Delta$  resonances is evident in Fig. 15, which shows the  $m_t - m_0$  spectra of pions near midrapidity ( $|y| < 0.3$ ) from RQMD. Pions whose last collision was a  $\Delta$  are plotted separately from the pions with all other last interactions. The spectral shapes are strongly affected by a  $\Delta$  lastcl. Plotted in Fig. 16 are the ratios of the pion yields from  $\Delta$ ’s and all other last interactions to the total yields as a function of  $m_t - m_0$ . In

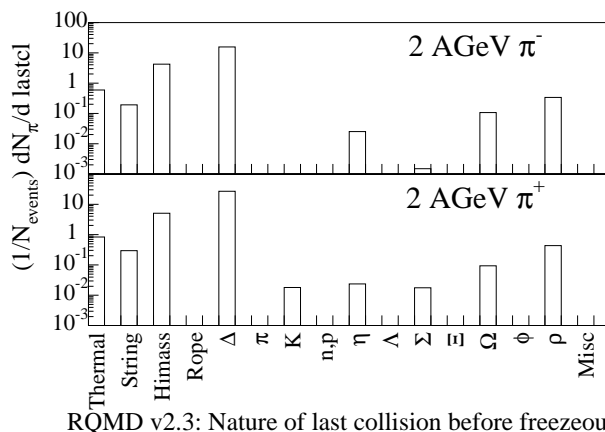


FIG. 13. RQMD nature of pion last collision, “lastcl,” before freeze-out at 2A GeV for impact parameter,  $b \leq 3$  fm.

all cases the  $\Delta$  pions contribute more significantly to the total yield at low  $m_t - m_0$  than at high  $m_t - m_0$ , but the influence of the  $\Delta$  contribution to the spectra diminishes as the beam energy increases. The total midrapidity pion spectra are fit with the same model as was used to describe the data, Eq. (3), with the fit parameters shown in Tables III and IV. At both high and low  $m_t - m_0$ , the RQMD  $\pi^-$  and  $\pi^+$  appear to have common inverse slope parameters and there is no obvious evolution with beam energy. The average value at low  $m_t - m_0$  ( $T_1$ ) is  $\sim 72$  MeV, while the high  $m_t - m_0$  ( $T_2$ ) average is  $\sim 140$  MeV. The magnitude of the low  $m_t - m_0$  RQMD inverse slope parameters is much larger than what is observed in the data at all beam energies. At high  $m_t - m_0$ , the RQMD inverse slope parameters are much closer to the observed values, except at 2A GeV, where the data show  $T_2 \sim 120$  MeV at midrapidity.

The rapidity density distributions of charged pions predicted by RQMD are shown in Fig. 17 alongside the E895 data from Figs. 7–11. The contributions to the total  $dN/dy$  from  $\Delta$  resonance decay pions and all other pions are also shown. As the beam energy increases, the contribution to the total from  $\Delta$  resonance decay pions becomes less important, which is consistent with the trends seen in the data.

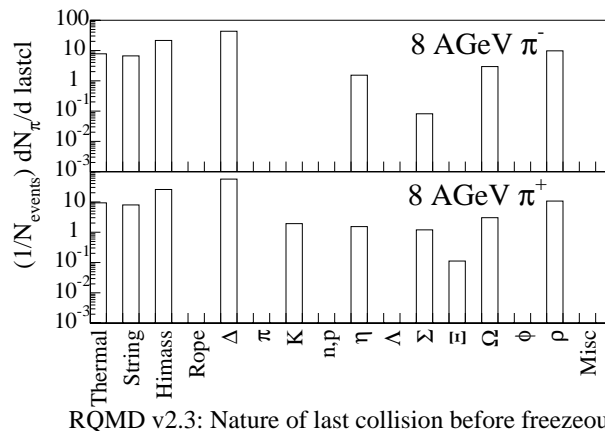


FIG. 14. RQMD nature of pion last collision, “lastcl,” before freeze-out at 8A GeV for impact parameter,  $b \leq 3$  fm.

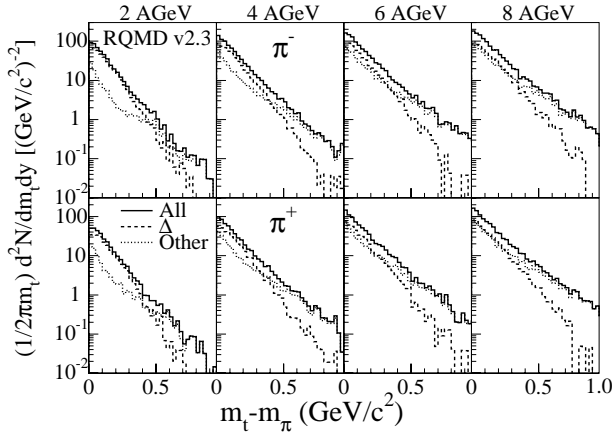


FIG. 15. RQMD charged pion spectra at midrapidity for collisions with impact parameter,  $b \leq 3$  fm. The contribution to the spectra from pions whose last interaction was a  $\Delta$  decay and the sum of all other processes are shown separately.

### B. Longitudinal flow

An important question in heavy ion collisions is the degree of collectivity of the produced particles, which can arise from the buildup of pressure in the hot, dense collision zone. RQMD has no such hydrodynamic effect explicitly included. However, individual particle thermal rescattering, the microscopic analog to pressure, can also drive collective flow, and has been observed in RQMD calculations at RHIC energies [43]. Rapidity broadening along the beam axis has been observed in heavy ion collisions at many beam energies for a wide range of systems and particle species [31,22,44,23]. This broadening has been interpreted as arising from the collective motion of the system in the longitudinal direction (longitudinal flow) after collision. The observed rapidity distributions are compared with the expectation for a stationary thermal source, and with a longitudinally boost-invariant superposition of multiple boosted individual isotropic, locally thermalized sources in a given rapidity interval. Each locally thermalized source is modeled by the  $m_T$ -integrated Maxwell-Boltzmann distribution, Eq. (1), with the rapidity dependence of the energy  $E = m_T \cosh(y)$  explicitly included, and  $T$  is true temperature:

$$\frac{dN_{th}}{dy}(y) = BT^3 \left( \frac{m^2}{T^2} + \frac{m}{T} \frac{2}{\cosh y} + \frac{2}{\cosh^2 y} \right) e^{(-m/T \cosh y)}. \quad (5)$$

The distributions are integrated over source element rapidity to extract the maximum longitudinal flow  $\eta_{max}$ ,

$$\frac{dN}{dy} = \int_{\eta_{min}}^{\eta_{max}} d\eta \frac{dN_{th}}{dy}(y - \eta), \quad (6)$$

$$\beta_L = \tanh(\eta_{max}),$$

where  $\eta_{max} = -\eta_{min}$ , from symmetry about the center of mass, and  $\beta_L$  is the maximum longitudinal velocity. An average longitudinal flow velocity can be defined as  $\langle \beta_L \rangle = \tanh(\eta_{max}/2)$ .

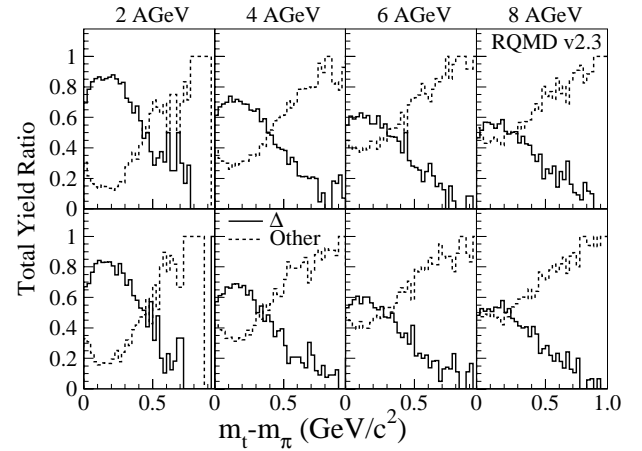


FIG. 16. Ratios of pion yield for different production mechanisms to the total yield as a function of  $m_1 - m_0$  at midrapidity from RQMD collisions with impact parameter,  $b \leq 3$  fm. The contribution to the spectra from pions whose last interaction was a  $\Delta$  decay and from the sum of all other processes are shown separately.

Reference [23] presents longitudinal flow velocities extracted from the proton rapidity densities measured by E895 for the same event selection as the pions presented in this analysis and compares the results to values extracted from a wide array of experiments over the beam energy range from 1A to 160A GeV. Since the protons are present before the collision, at higher beam energies they may be strongly affected by nuclear transparency, which can also broaden the rapidity distributions. Therefore, the protons alone cannot be used to determine the absolute magnitude of the collective motion, if it is present.

In order to determine the degree of collectivity, it is important to compare multiple particle species from the same collisions simultaneously. This has been done with central Si+Al collisions at 14.6 A GeV for protons, pions, kaons, and  $\Lambda$  hyperons [44] and in central S+S collisions at 200 AGeV for pions, kaons and  $\Lambda$  hyperons [31]. A common collective flow velocity was able to reasonably describe all of the observed rapidity distributions, except the protons in S+S collisions at 200A GeV. A similar simultaneous description is possible here, by combining the proton rapidity distributions from Ref. [23] with the present pion rapidity distributions.

The rapidity densities of pions and the protons from Ref. [23] are shown in Fig. 18. Stationary thermal source emission functions, the sum of two of Eq. (5) for the pions using the two inverse slope parameters from the pion transverse mass spectra fits at midrapidity, are shown as dashed lines.

TABLE III. Midrapidity RQMD  $\pi^-$  fit parameters, Eq. (3).

| $E_{beam}$ (A GeV) | $dN/dy_1$ | $T_1$ (MeV/c <sup>2</sup> ) | $dN/dy_2$ | $T_2$ (MeV/c <sup>2</sup> ) |
|--------------------|-----------|-----------------------------|-----------|-----------------------------|
| 2                  | 17.4      | 73                          | 1.8       | 146                         |
| 4                  | 21.3      | 73                          | 10.9      | 131                         |
| 6                  | 26.6      | 74                          | 15.5      | 146                         |
| 8                  | 31.7      | 77                          | 20.1      | 155                         |

TABLE IV. Midrapidity RQMD  $\pi^+$  fit parameters, Eq. (3).

| $E_{beam}$ (A GeV) | $dN/dy_1$ | $T_1$ (MeV/c <sup>2</sup> ) | $dN/dy_2$ | $T_2$ (MeV/c <sup>2</sup> ) |
|--------------------|-----------|-----------------------------|-----------|-----------------------------|
| 2                  | 10.2      | 73                          | 1.6       | 134                         |
| 4                  | 14.4      | 72                          | 8.5       | 131                         |
| 6                  | 15.5      | 64                          | 17.7      | 131                         |
| 8                  | 21.4      | 70                          | 21.3      | 144                         |

We have not measured the true system temperature  $T$ , since  $T_1$  and  $T_2$  parametrize the temperature and known radial flow, resonance and Coulomb effects in the pion spectra. Consequently,  $T_2$  overestimates the system temperature and  $T_1$  may underestimate (due to competing effects of radial flow, resonance feed-down, and the Coulomb interaction with the fireball). Therefore the plotted distributions (dashed lines) are probably wider than the true thermal distributions would be, and yet are still too narrow to reproduce the observed rapidity spectra. The inclusion of longitudinal flow remedies this. For the protons, a single Eq. (5) is used for the thermal rapidity distribution, as in Ref. [23].

The solid curves are the emission functions including longitudinal flow, Eq. (6), with the velocities fixed to the values extracted from the protons ( $\langle\beta_L\rangle=0.28, 0.42, 0.48, 0.50$  at 2A, 4A, 6A, and 8A GeV respectively). The longitudinally expanding source clearly better reproduces the measured pion distributions at all beam energies than do the dashed curves in Fig. 18. Consistency among particles of different masses supports a hydrodynamical interpretation of the rapidity density broadening; the system is expanding like a fluid with a common longitudinal flow velocity.

### C. Entropy production

It was suggested many years ago by Fermi [45] and later Landau [46] that pion production may be used to estimate

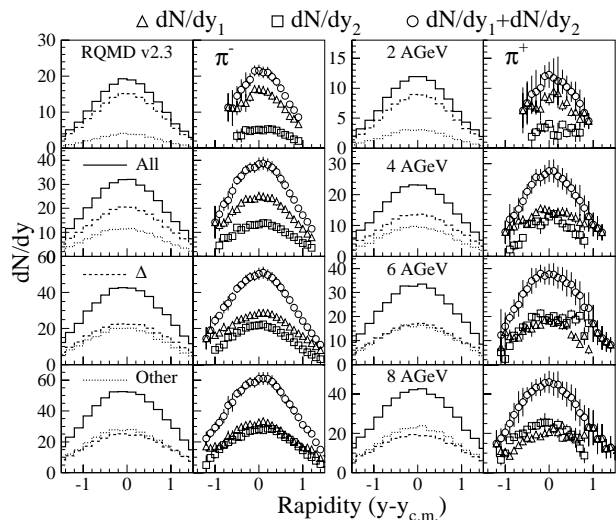


FIG. 17. Rapidity density of charged pions from RQMD calculations for collisions with impact parameter,  $b \leq 3$  fm. The contribution from  $\Delta$  resonance decay pions and the sum of all other processes are also plotted separately to show the relative contribution to the pion yields from  $\Delta$  decays. For comparison, the data from Figs. 7–11 are also shown.

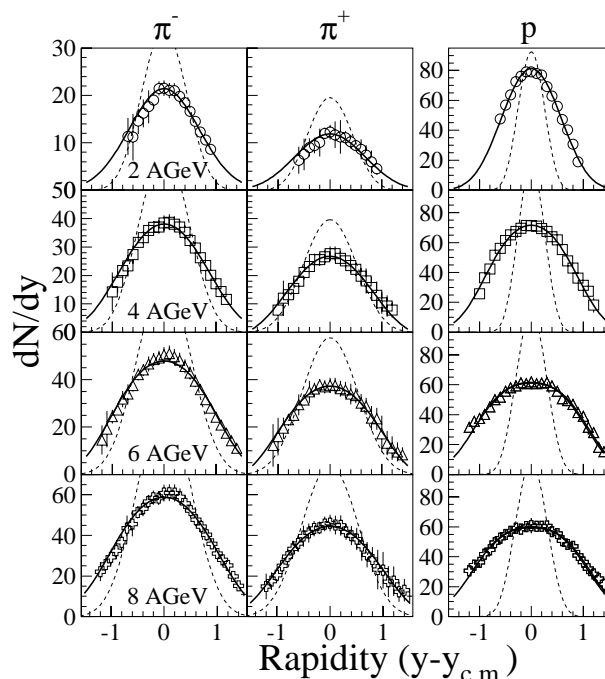


FIG. 18.  $\pi^-$ ,  $\pi^+$ , and proton rapidity density distributions at 2A, 4A, 6A, and 8A GeV. The expectation for isotropic emission from a stationary thermal source is indicated with dashed lines, whereas the solid curves represent the form including longitudinal flow from the proton  $\eta_{max}$  values given in Ref. [23]. In all cases the thermal model is too narrow. The proton data and the longitudinal expansion velocity come from Ref. [23].

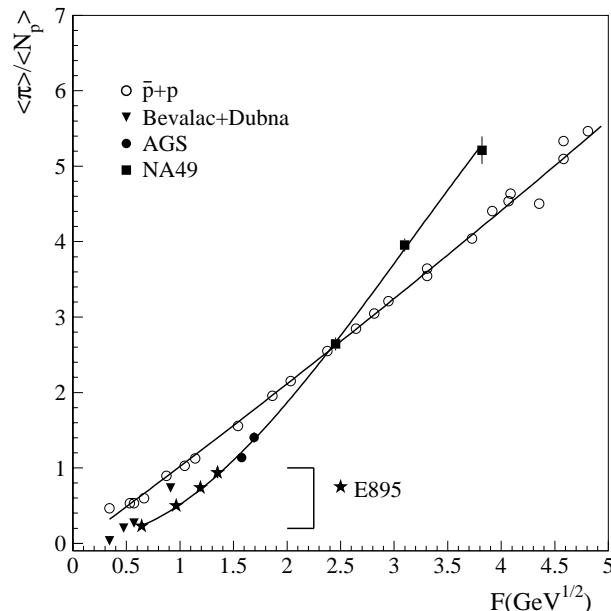


FIG. 19. Mean pion multiplicity per participant vs  $F$ , the Fermi energy variable. The solid symbols represent data from heavy ion collisions, whereas the open symbols come from  $p+p$  interactions. The E895 data points are indicated by stars. The third-order polynomial fit to the heavy ion data shows that a smooth trend with  $F$  is possible, although the low energy and high energy data (including RHIC results) can be well described by separate linear parametrizations whose slopes differ by a factor of  $\approx 1.3$  [24].

the amount of entropy produced in high energy particle collisions. Later, Van Hove [47] extended this idea to heavy ion collisions and proposed that this may be a way to distinguish events in which a QGP is formed. In a QGP the color degrees of freedom of the liberated partons introduce a significant number of new energy states unavailable in a hadron gas. By studying pion production over a broad range of collision systems and energies, discontinuities in the observed multiplicities might indicate the onset of QGP formation.

In 1995, Gaździcki [48] took the available data from heavy ion collisions and showed that there is an increase in the observed entropy produced at the SPS (NA35 experiment with S+S collisions at 200A GeV [49]) compared with AGS energies. The low energy heavy ion data follow the trend for  $p+p$  collisions, while at the SPS there is an apparent factor of 3 increase in the effective number of degrees of freedom [50]. The entropy production analysis of Pb+Pb collisions at 158A GeV (NA49) [51] supported this observation.

This model assumes that the entropy is produced at the early stage of the collision when the incident matter is in a highly excited state. The thermalized, strongly interacting matter is assumed to expand adiabatically to the freeze-out point, preserving the early stage entropy.

Since the majority of produced particles are pions, to first order, the mean pion (boson) multiplicity should be nearly proportional to the entropy. The ratio of the mean pion multiplicity to the mean number of participating nucleons,  $\langle\pi\rangle/\langle N_p\rangle$ , provides a simple estimate of the entropy density.  $\langle N_p\rangle$  for a nucleus-nucleus collision can be estimated using a Glauber model calculation of the mean free path of the nucleons through the nuclei as they collide at a given impact parameter. For the present analysis,  $\langle N_p\rangle$  was estimated using RQMD. The nucleons are distributed according to a Woods-Saxon nuclear density profile and the impact parameter of the simulated collision is used with the nucleon-nucleon interaction cross sections [52] to determine the number of participants. The top 5% of collisions (determined by integrating the  $\langle N_p\rangle$  distribution from a set of minimum bias RQMD events at each beam energy) correspond to  $\langle N_p\rangle=364, 366, 365, 363$  at 2A, 4A, 6A, and 8A GeV, respectively. The estimated uncertainty on these values is  $\pm 5$  participants.

Following Ref. [24], the entropy densities for each beam energy, here approximated as  $\langle\pi\rangle/\langle N_p\rangle$ , with  $\langle\pi\rangle=1.5(\langle\pi^-\rangle+\langle\pi^+\rangle)$  to account for the neutral pions, are plotted in Fig. 19 as a function of the Fermi energy variable,  $F\equiv(\sqrt{s_{NN}}-2m_N)^{3/4}/\sqrt{s_{NN}}^{1/4}$ . E895 data are indicated by stars and the values are tabulated in Table V. NA49 results for 40A, 80A, and 158A GeV Pb+Pb collisions from the CERN SPS were obtained from Ref. [24]. The number of participants from Ref. [24], calculated using the Fritiof [53] model, are also listed in Table V.

The linear dependence of the entropy per participant nucleon as a function of  $F$  in the proton-proton ( antiproton) data is not evident for the full range of the heavy ion collision data. At and below AGS energies, the heavy ion data lie below the  $p+p$  data, and appear to be approximately linear with  $F$ . In Ref. [24], the SPS results combined with RHIC results at much higher energies from the PHOBOS Collaboration show a linear trend with a slope that is  $\approx 1.3$  times

TABLE V. Tabulated mean number of pions per participant and Fermi energy variable for 2A, 4A, 6A, and 8A GeV Au+Au collisions and 40A, 80A, and 158A GeV Pb+Pb collisions from Ref. [24]. Statistical and systematic uncertainties are reported separately.

| $\sqrt{s_{NN}}$ (GeV) | $F$ (GeV <sup>1/2</sup> ) | $\langle N_p\rangle$ | $\langle\pi\rangle/\langle N_p\rangle$ |
|-----------------------|---------------------------|----------------------|--|
| 2.630                 | 0.644                     | 364                  | $0.2279\pm 0.0159^{+0.0124}_{-0.0165}$ |
| 3.279                 | 0.965                     | 366                  | $0.5012\pm 0.0111^{+0.0307}_{-0.0357}$ |
| 3.838                 | 1.190                     | 365                  | $0.7385\pm 0.0148^{+0.0341}_{-0.0362}$ |
| 4.289                 | 1.351                     | 363                  | $0.9364\pm 0.0170^{+0.0570}_{-0.0579}$ |
| 8.830                 | 2.452                     | 349                  | $2.6433\pm 0.0858$                     |
| 12.280                | 3.099                     | 349                  | $3.9542\pm 0.0869$                     |
| 17.260                | 3.821                     | 362                  | $5.2127\pm 0.1823$                     |

larger than at the lower energies. There appears to be a transition in the region between the AGS and top SPS energies. The third-order polynomial fit to the heavy ion data shown on Fig. 19 may indicate that a smooth trend with increasing  $F$  can accurately describe the excitation function without the need for a discontinuous jump, such as one might expect from a first-order phase transition. Two more runs at the SPS with beam energies of 20A GeV and 30A GeV may be able to improve the resolution in this important transition region.

## V. SUMMARY

Transverse mass and rapidity spectra of charged pions in 2–8A GeV 0–5% central Au+Au collisions have been measured by the E895 experiment. The transverse mass spectra exhibit a low- $p_t$  enhancement which can be largely ascribed to the feed-down from late-stage resonance decays. Differences in the  $\pi^+$  and  $\pi^-$  spectra at low  $m_t-m_0$  are not reproduced by RQMD, which does not include final-state interactions such as the Coulomb interaction with the nuclear source. The inverse slope parameters increase as a function of beam energy and appear to be charge independent at high  $m_t-m_0$ . The measured rapidity distributions show excellent forward-backward rapidity symmetry and are well described by a model that includes collective longitudinal flow, with a velocity that is common to both pions and protons emitted in these collisions. The  $4\pi$  yields of pions, obtained by integrating the rapidity distributions, have been used to infer an initial-state entropy which increases with beam energy and is consistent with a smooth nonlinear trend as a function of  $F$  from the 2A GeV Au+Au collisions to 158A GeV Pb+Pb collisions at the SPS.

## ACKNOWLEDGMENTS

This work was supported in part by the U.S. Department of Energy under Grant Nos. DE-FG02-87ER40331.A008, DE-FG02-89ER40531, DE-FG02-88ER40408, DE-FG02-87ER40324, and Contract No. DE-AC03-76SF00098; by the US National Science Foundation under Grant Nos. PHY-98-04672, PHY-9722653, PHY-96-05207, PHY-9601271, and PHY-9225096; and by the University of Auckland Research Committee, NZ/USA Cooperative Science Programme CSP 95/33.

- [1] M. A. Lisa *et al.*, EOS Collaboration, Phys. Rev. Lett. **75**, 2662 (1995).
- [2] N. Herrmann *et al.*, FOPI Collaboration, Nucl. Phys. **A610**, 49c (1996).
- [3] L. Ahle *et al.*, E802 Collaboration, Phys. Rev. C **57**, R466 (1998).
- [4] J. Barrette *et al.*, E877 Collaboration, Phys. Rev. C **62**, 024901 (2000).
- [5] H. Stöcker and W. Greiner, Phys. Rep. **137**, 277 (1986).
- [6] G. F. Bertsch and S. Das Gupta, Phys. Rep. **160**, 189 (1988).
- [7] S. J. Wang, B. A. Li, W. Bauer, and J. Randrup, Ann. Phys. (San Diego) **209**, 251 (1991).
- [8] B. A. Li and K. M. Ko, Phys. Rev. C **52**, 2037 (1995).
- [9] C. Pinkenburg *et al.*, E895 Collaboration, Phys. Rev. Lett. **83**, 1295 (1999).
- [10] H. Liu *et al.*, E895 Collaboration, Phys. Rev. Lett. **84**, 5488 (2000).
- [11] S. Nagamiya *et al.*, Phys. Rev. C **24**, 971 (1981).
- [12] H. Ströbele *et al.*, Phys. Rev. C **27**, 1349 (1983).
- [13] R. Stock, Phys. Rep. **135**, 259 (1986).
- [14] P. Danielewicz, Phys. Rev. C **51**, 716 (1995).
- [15] H. Stöcker, J. Phys. G **6**, L111 (1984).
- [16] D. Pelte *et al.*, FOPI Collaboration, Z. Phys. A **357**, 215 (1997).
- [17] A. Wagner *et al.*, Phys. Lett. B **420**, 20 (1998).
- [18] L. B. Venema *et al.*, Phys. Rev. Lett. **71**, 835 (1993).
- [19] O. Schwalb *et al.*, Phys. Lett. B **321**, 20 (1994).
- [20] H. Sorge, Phys. Rev. C **49**, R1253 (1994).
- [21] J. Barrette *et al.*, E877 Collaboration, Phys. Lett. B **351**, 93 (1995).
- [22] J. Stachel, Nucl. Phys. **A610**, 509c (1996).
- [23] J. L. Klay *et al.*, E895 Collaboration, Phys. Rev. Lett. **88**, 102301 (2002).
- [24] S. V. Afanasiev *et al.*, NA49 Collaboration, Phys. Rev. C **66**, 054902 (2002).
- [25] G. Rai *et al.*, IEEE Trans. Nucl. Sci. **37**, 56 (1990).
- [26] C. Cavata *et al.*, Phys. Rev. C **42**, 1760 (1990).
- [27] L. Ahle *et al.*, E866/E917 Collaborations, Nucl. Phys. **A638**, 57c (1998).
- [28] J. C. Dunlop, Ph.D. Dissertation, Massachusetts Institute of Technology, 1999.
- [29] R. Seto *et al.*, E917 Collaboration, Nucl. Phys. **A638**, 407c (1998).
- [30] L. Ahle *et al.*, E866/E917 Collaborations, Phys. Lett. B **476**, 1 (2000).
- [31] Ekkard Schnedermann, Josef Sollfrank, and Ulrich Heinz, Phys. Rev. C **48**, 2462 (1993).
- [32] Josef Sollfrank, Peter Koch, and Ulrich Heinz, Phys. Lett. B **252**, 256 (1990).
- [33] M. Hofmann, R. Mattiello, H. Sorge, H. Stöcker, and W. Greiner, Phys. Rev. C **51**, 2095 (1995).
- [34] W. Weinhold, B. Friman, and W. Nörenberg, Phys. Lett. B **433** (1998).
- [35] M. Gyulassy and S. K. Kauffmann, Nucl. Phys. **A362**, 503 (1981).
- [36] H. W. Barz, J. P. Bondorf, J. J. Gaardhøje, and H. Heiselberg, Phys. Rev. C **57**, 2536 (1998).
- [37] A. Ayala, S. Jeon, and J. Kapusta, Phys. Rev. C **59**, 3324 (1999).
- [38] J. W. Dunn, Ph.D. Dissertation, University of California, Davis, 1997.
- [39] B. J. VerWest and R. A. Arndt, Phys. Rev. C **25**, 1979 (1982).
- [40] H. Sorge, Phys. Rev. C **52**, 3291 (1995).
- [41] S. A. Bass *et al.*, Prog. Part. Nucl. Phys. **41**, 225 (1998).
- [42] N. Xu *et al.*, NA44 Collaboration, Nucl. Phys. **A610**, 175c (1996).
- [43] B. Monreal, W. J. Llope, R. Mattiello, S. Y. Panitkin, H. Sorge, and N. Xu, Phys. Rev. C **60**, 051902 (1999).
- [44] P. Braun-Munzinger, J. Stachel, J. P. Wessels, and N. Xu, Phys. Lett. B **344**, 43 (1995).
- [45] E. Fermi, Prog. Theor. Phys. **5**, 570 (1950).
- [46] L. D. Landau, Izv. Akad. Nauk SSSR, Ser. Fiz. **17**, 51 (1953).
- [47] L. Van Hove, Phys. Lett. **118B**, 138 (1982).
- [48] Marek Gaździcki and Dieter Rörich, Z. Phys. C **65**, 215 (1995).
- [49] J. Bächler *et al.*, NA35 Collaboration, Phys. Rev. Lett. **72**, 1419 (1994).
- [50] Marek Gaździcki, Z. Phys. C **66**, 659 (1995).
- [51] P. Brady and J. Dunn, Eur. Phys. J. C **5**, 357 (1998).
- [52] Particle Data Group, L. Montanet *et al.*, Phys. Rev. D **50**, 1173 (1994).
- [53] B. Andersson, G. Gustafson, and Hong Pi, Z. Phys. C **57**, 485 (1993).